16

Applications in Numerical Modeling and Simulation

Chu et al. (1999a, b) investigates two kinds of predictability in the Lorenz system: uncertain initial condition (first kind) and uncertain external forcing (second kind). Similarly, the first kind ocean model predictability is due to uncertain initial condition, and the second kind ocean model predictability is due to uncertain lateral boundary condition and atmospheric forcing. Since the P-vector inverse method computes absolute velocity from (T, S) data, it can be used to overcome difficulties such as uncertain initial velocity field and open boundary condition. Besides, it can also be incorporated with (T, S) data assimilation system such as MODAS to establish a quick ocean environmental assessment system.

16.1 Velocity Initialization

Ocean modeling aims to integrate hydrodynamic and thermodynamic equations numerically with boundary conditions (lateral and vertical) from initial states of temperature (T), salinity (S), and velocity. Initial T, S fields are relatively easy to obtain, such as using climatological such as (WOA, GDEM) or synoptic data set such as MODAS (T_c, S_c). However, the initial velocity field is usually not available due to insufficient number of velocity observations. Thus, initialization of the velocity field becomes an important procedure for ocean modeling.

Diagnostic initialization is widely used. It integrates the model from known temperature (T_c) and salinity (S_c) and zero velocity fields while holding (T_c, S_c) unchanged. After a period (around 30 days) of the diagnostic run, the velocity field $(\mathbf{V}_c)$ is established, and $(T_c, S_c, \mathbf{V}_c)$ fields are then treated as the initial conditions for the prognostic numerical modeling. Chu and Wang (2003) show that during the diagnostic initialization period, the heat and salt "source/sink" terms are generated at each time step, and therefore it is not suitable for ocean modeling.

16.1.1 Initial Condition for Velocity in Ocean Models

Let $(\mathbf{V}_\mathrm{h}, w)$ be the horizontal and vertical velocity components, and ∇ the horizontal gradient operator. Ocean numerical models are based on the momentum equation

$$\frac{\partial \mathbf{V}_\mathrm{h}}{\partial t} = -\mathbf{V}_\mathrm{h} \cdot \nabla \mathbf{V}_\mathrm{h} - w \frac{\partial \mathbf{V}_\mathrm{h}}{\partial z} - \mathbf{k} \times f \mathbf{V}_\mathrm{h} - \frac{1}{\rho} \nabla p + \frac{\partial}{\partial z} \left(K_\mathrm{M} \frac{\partial \mathbf{V}_\mathrm{h}}{\partial z} \right) + \mathbf{H_V}, \quad (16.1a)$$

and the temperature and salinity equations,

$$\frac{\partial T}{\partial t} = -\mathbf{V}_\mathrm{h} \cdot \nabla T - w \frac{\partial T}{\partial z} + \frac{\partial}{\partial z} \left(K_\mathrm{H} \frac{\partial T}{\partial z} \right) + H_\mathrm{T}, \quad (16.1b)$$

$$\frac{\partial S}{\partial t} = -\mathbf{V}_\mathrm{h} \cdot \nabla S - w \frac{\partial S}{\partial z} + \frac{\partial}{\partial z} \left(K_\mathrm{H} \frac{\partial S}{\partial z} \right) + H_\mathrm{S}, \quad (16.1c)$$

where $(K_\mathrm{M}, K_\mathrm{H})$ are the vertical eddy diffusivity for turbulent mixing of momentum, temperature, and salinity. The terms $(\mathbf{H_v}, H_\mathrm{T}, H_\mathrm{S})$ represent the subgrid processes causing the local time rate of change in $(\mathbf{V}_\mathrm{h}, T, S)$.

In ocean modeling practice, climatological $(T_\mathrm{c}, S_\mathrm{c})$ data are usually taken as the initial (T, S) conditions. The climatological data may represent long term equilibrium state,

$$\frac{\partial T_\mathrm{c}}{\partial t} \approx 0, \quad \frac{\partial S_\mathrm{c}}{\partial t} \approx 0.$$

The vertical and horizontal diffusions are also small for the $(T_\mathrm{c}, S_\mathrm{c})$ fields. Thus, we have

$$\mathbf{V}_\mathrm{h} \cdot \nabla T_\mathrm{c} + w \frac{\partial T_\mathrm{c}}{\partial z} = 0, \quad \mathbf{V}_\mathrm{h} \cdot \nabla S_\mathrm{c} + w \frac{\partial S_\mathrm{c}}{\partial z} = 0, \quad (16.2)$$

which leads to

$$\mathbf{V} \cdot \nabla \rho = 0, \quad (16.3)$$

where $\mathbf{V} \equiv (\mathbf{V}_\mathrm{h}, w)$ is the three-dimensional absolute velocity.

The inverted absolute velocity using the P-vector method has the property described by (16.3). This implies that when the absolute velocity calculated using the P-vector method $(\mathbf{V}^{(\mathrm{p})})$ is taken as the initial condition along with $(T_\mathrm{c}, S_\mathrm{c})$, the heat and salt (16.1b, c) are generally satisfied at $t = 0$.

16.1.2 Weakness of the Diagnostic Initialization

The widely used model initialization is the diagnostic mode, which integrates the model from known T, S data such as climatological $(T_\mathrm{c}, S_\mathrm{c})$ and zero velocity fields, while holding $(T_\mathrm{c}, S_\mathrm{c})$ unchanged. After a period (about 30 days) of the diagnostic run, the velocity field $(\mathbf{V}_\mathrm{c}, w_\mathrm{c})$ is established, and

$(T_c, S_c, \mathbf{V}_c, w_c)$ fields are treated as the initial conditions for numerical prognostic modeling. Since initial condition error drastically affects model predictability (Lorenz 1963; Chu 1999a, b), questions arise: Does the diagnostic mode provide ideal initialization? What is the physical process associated with the diagnostic run? Chu and Lan (2003) found extra large nonphysical source/sink terms generated using the diagnostic initialization.

The diagnostic initialization procedure integrates (16.1a, b, c) from

$$T = T_c, \quad S = S_c, \quad \mathbf{V} = 0, \quad \text{at } t = 0, \tag{16.4}$$

with T and S unchanged. This procedure is analogous to the process of adding heat and salt source/sink terms (F_T, F_S) in (16.2) and (16.3)

$$\frac{\partial T}{\partial t} = -\mathbf{V} \cdot \nabla T - w\frac{\partial T}{\partial z} + \frac{\partial}{\partial z}\left(K_H \frac{\partial T}{\partial z}\right) + H_T + F_T, \tag{16.5}$$

$$\frac{\partial S}{\partial t} = -\mathbf{V} \cdot \nabla S - w\frac{\partial S}{\partial z} + \frac{\partial}{\partial z}\left(K_H \frac{\partial S}{\partial z}\right) + H_S + F_S, \tag{16.6}$$

to keep

$$\frac{\partial T}{\partial t} = 0, \quad \frac{\partial S}{\partial t} = 0, \tag{16.7}$$

at the each time step (diagnostic initialization). Comparison of (16.7) with (16.5) and (16.6) yields

$$F_T \equiv \mathbf{V} \cdot \nabla T + w\frac{\partial T}{\partial z} - \frac{\partial}{\partial z}\left(K_H \frac{\partial T}{\partial z}\right) - H_T, \tag{16.8}$$

$$F_S \equiv \mathbf{V} \cdot \nabla S + w\frac{\partial S}{\partial z} - \frac{\partial}{\partial z}\left(K_H \frac{\partial S}{\partial z}\right) - H_S. \tag{16.9}$$

Usually, $F_T \neq 0, F_S \neq 0$, thus, the heat and salt "source/sink" terms are generated during the diagnostic initialization at each time step.

16.1.3 Measures of "Source/Sink" Strength

Most diagnostic initialization uses the climatologically monthly (or annual) mean data as the initial T, S conditions. The maximum variability of T, S is estimated by 35°C and 35 ppt. Thus, maximum time rates of absolute change of the monthly mean T, S data (usually taken as initial conditions) are estimated by

$$\left|\frac{\partial T}{\partial t}\right| \leq 35°\text{C year}^{-1} \simeq 0.1°\text{C day}^{-1}, \quad \left|\frac{\partial S}{\partial t}\right| \leq 35\,\text{ppt year}^{-1} \simeq 0.1\,\text{ppt day}^{-1}. \tag{16.10}$$

These values may represent standard measures for "sources/sinks". Twenty-four times of the standard measures

$$\left|\frac{\partial T}{\partial t}\right|_{\text{Strong}} \simeq 0.1^\circ\text{C}\,\text{h}^{-1}, \quad \left|\frac{\partial S}{\partial t}\right|_{\text{Strong}} \simeq 0.1\,\text{ppt}\,\text{h}^{-1}, \tag{16.11}$$

represent strong "sources/sinks". Ten times of the strong "sources/sinks" $|\partial T/\partial t|_{\text{Strong}}$ and $|\partial S/\partial t|_{\text{Strong}}$,

$$\left|\frac{\partial T}{\partial t}\right|_{\text{Extra Strong}} \simeq 1^\circ\text{C}\,\text{h}^{-1}, \quad \left|\frac{\partial S}{\partial t}\right|_{\text{Extra Strong}} \simeq 1\,\text{ppt}\,\text{h}^{-1}, \tag{16.12}$$

represent extremely strong "sources/sinks".

Question arises: how large are these source/sink terms after the initialization? Are the false "sources/sinks" bearable for numerical modeling? The Princeton Ocean Model (POM) implemented for the Japan Sea is used to evaluate the magnitude of the source/sink terms after the diagnostic initialization.

16.1.4 POM for the Japan/East Sea

The POM for the Japan/East Sea is used to illustrate the generation of numerically generated (nonphysical) extremely strong thermohaline source/sink terms. Information about the Japan Sea geography and oceanography can be found in Sect. 6.5.1. The smoothed bathymetry is shown in Fig. 16.1.

The Japan/East Sea model contains 94×100 horizontally fixed grid points with horizontal spacing of $10'$ latitude and longitude (approximately 11.54–15.18 km in the zonal direction and 18.53 km in the latitudinal direction) and 15 vertical nonuniform sigma coordinate levels. The model domain is from 35.0 to 52°N, and from 127.0 to 142.5°E. The bottom topography is obtained from the smoothed Naval Oceanographic Office Digital Bathymetry Data Base 5 min resolution. The horizontal diffusivities are modeled using the Smagorinsky form with the coefficient chosen to be 0.2 for this application. No atmospheric forcing is applied to the model. Closed lateral boundaries, i.e., the modeled ocean bordered by land, were defined using a free-slip condition for velocity and a zero gradient condition for temperature and salinity. No advective or diffusive heat, salt or velocity fluxes occur through these boundaries. At open boundaries, we use the radiative boundary condition with zero volume transport.

For computational efficiency, the mode splitting technique (Blumberg and Mellor 1987) is applied with a barotropic time step of 24 s, based on the Courant-Friedrichs-Levy (CFL) computational stability condition and the external wave speed; and a baroclinic time step of 720 s, based on the CFL condition and the internal wave speed.

The annual mean GDEM T, S data are used for the study. Here, the fields at the surface and 150 m depth are presented. The depth of 150 m corresponds
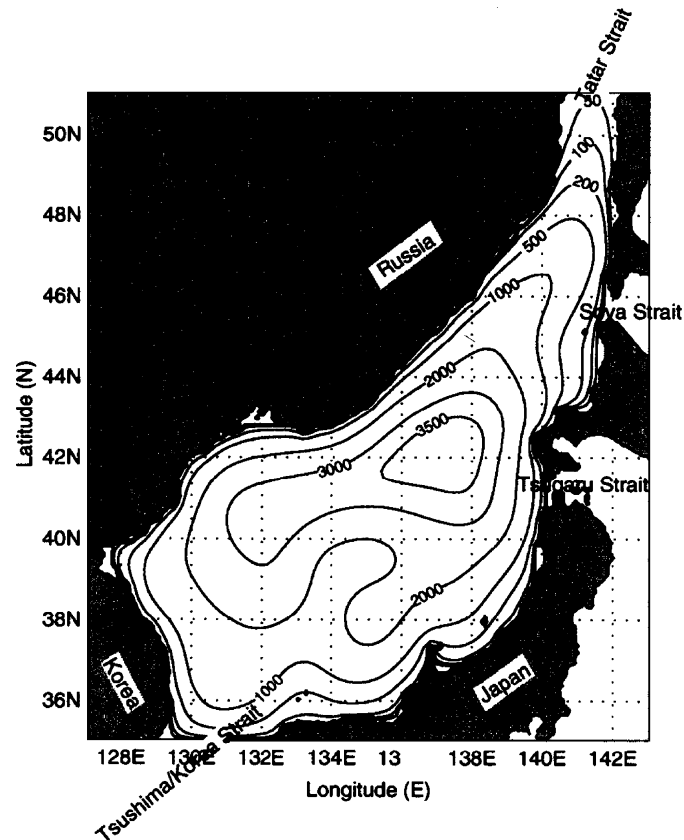
Fig. 16.1. Geography and isobaths showing the bottom topography of the Japan/East Sea model (from Chu and Wang 2003, Geophysical Research Letters)

to the permanent thermocline and the middle level of the Japan Sea Intermediate Water. Below the depth of 150 m, the water mass is quite uniform. Nonuniform heat/salt source and sink terms might cause abrupt thermohaline change.

The climatological mean temperature field at two depths (0, 150 m) clearly shows the existence of the Subpolar Front with the position around 38°N in the west and near 42°N in the east (Fig. 16.2a, b. The temperature is more than 6°C higher south of Subpolar Front than north of Subpolar Front at 0 and 150 m. The climatological mean salinity field at the surface (Fig. 16.2a) clearly shows that the saline Kuroshio water (>34.2 ppt) enters the Japan Sea from the Tsushima/Korean Strait into the Japan Sea and forms two permanent salty centers with the salinity higher than 34.0 ppt, located north of Subpolar Front (west of the Hokkaido Island) and south of Subpolar Front at $37-40°$N, $132-136°$E. Around the southern salty center, there are several fresh centers with the minimum salinity less than 33.9 ppt. The climatological
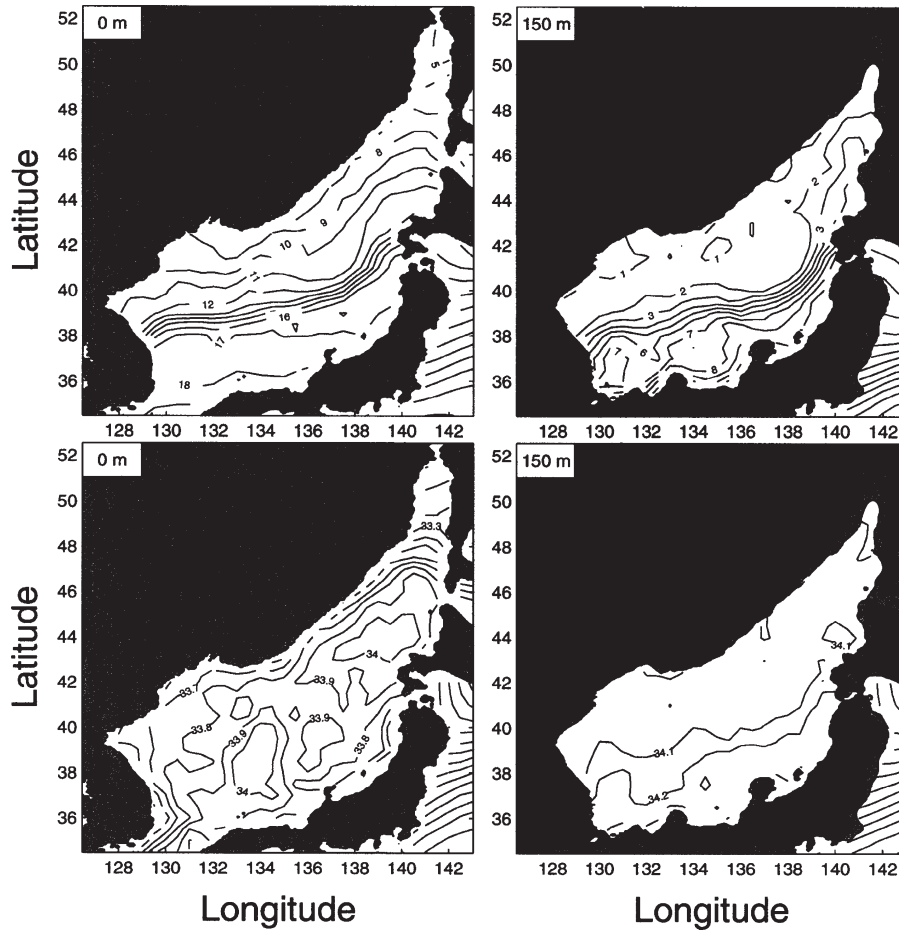
Fig. 16.2. GDEM annual mean (**a**) temperature and (**b**) salinity at various depths (from Chu and Wang 2003, Geophysical Research Letters)

mean salinity field at 150 m depth (Fig. 16.2b) clearly shows that the isohaline of 34.1 is colocated with the Subpolar Front (Fig. 16.2b) with the salinity above (below) 34.1 in the south (north) of the Subpolar Front. Salinity is more uniform north of than south of the Subpolar Front.

The POM was integrated in the diagnostic mode with all three components of velocity (u, v, w) initially set to zero, and with temperature and salinity specified by interpolating GDEM annual mean data to each model grid point.
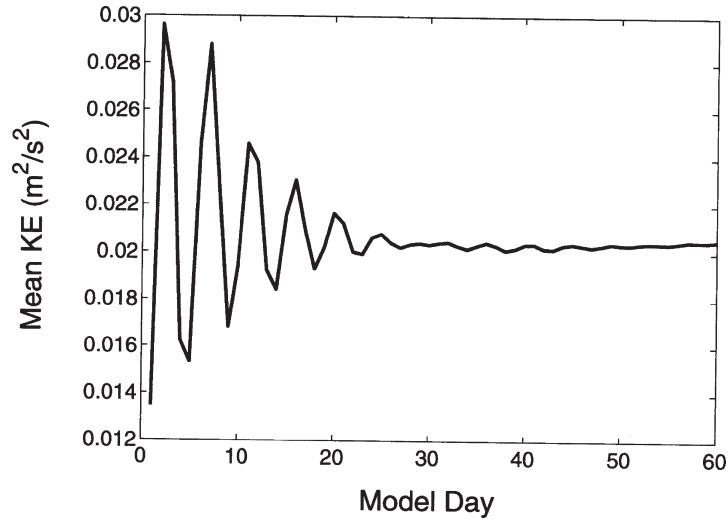
Fig. 16.3. Temporal variation of total kinetic energy. Note that the quasisteady state is reached after 30 day's integration (from Chu and Wang 2003, Geophysical Research Letters)

F_T and F_S are obtained at each time step. The diagnostic model was integrated for 60, 30 days were sufficient for the volume-mean model kinetic energy to reach quasisteady state under the imposed conditions (Fig. 16.3). The thermohaline source/sink terms (F_T, F_S) generated by the diagnostic initialization on day-30 and day-60 are used to identify their magnitudes and sensitivity to the integration period.

16.1.5 Extremely Strong Source/Sink Terms

Horizontal distributions of $\rho c_p F_T$ (unit: $\mathrm{W\,m^{-3}}$) on day-30 (Fig. 16.4) at the four σ levels $(0, -0.143, -0.5,$ and $-0.929)$ show extremely strong heat sources/sinks generated by the diagnostic initialization. For $\rho c_p F_T = 1,000\,\mathrm{W\,m^{-3}}$, the time rate of absolute temperature change $F_T = 0.84°\mathrm{C\,h^{-1}}$. The sources/sinks have various scales and strengths. They reveal small- to meso-scale patterns in most areas except a large-scale pattern near the bottom $(\sigma = -0.929)$. The strength of the source/sink increases with depth from the surface to subsurface. The extremely strong source reaching $5,164\,\mathrm{W\,m^{-3}}$ (corresponding to $F_T = 4.34°\mathrm{C\,h^{-1}}$) and the extremely strong sink reaching $-4,735\,\mathrm{W\,m^{-3}}$ (corresponding to $F_T = -3.98°\mathrm{C\,h^{-1}}$), and decreases with depth below the subsurface. Near the bottom, the Japan/East Sea basin is dominated by cooling with the maximum sink strength $-1,557\,\mathrm{W\,m^{-3}}$ (corresponding to $F_T = -1.31°\mathrm{C\,h^{-1}}$). From the subsurface to the bottom, the source/sink terms have some organized pattern near the Subpolar Front. At the subsurface, a dipole pattern occurs between 133 and 136°E with
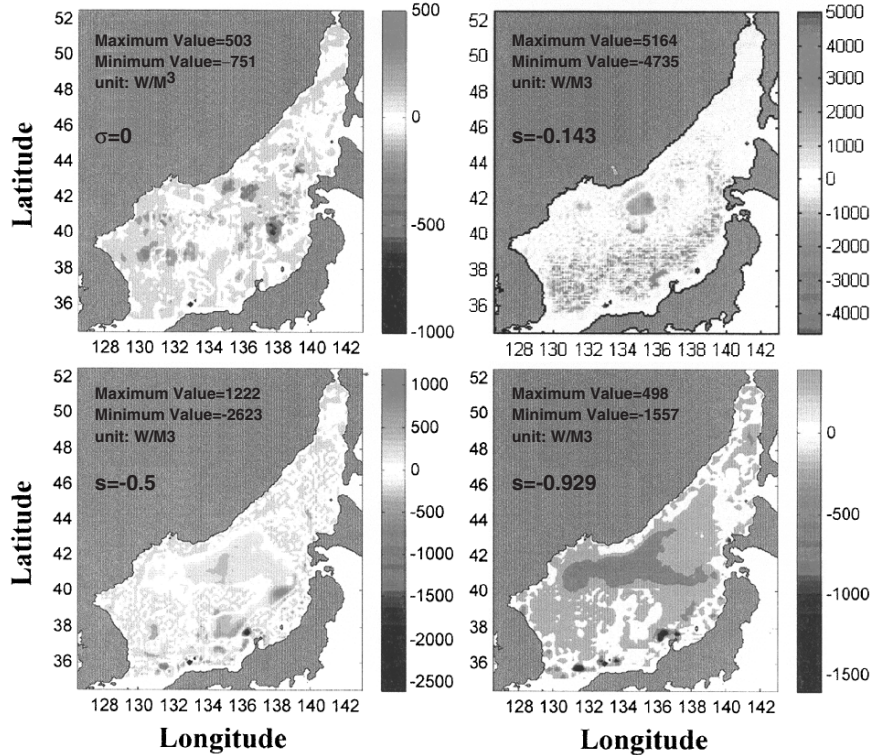
Fig. 16.4. Horizontal distribution of $\rho c_{\mathrm{p}} F_{\mathrm{T}}$ (unit: $\mathrm{W\,m^{-3}}$) on day-30 at σ levels of: (**a**) 0, (**b**) -0.143, (**c**) -0.5, and (**d**) -0.929 (from Chu and Lan 2003, Geophysical Research Letters)

strong source strength approximate $2,000\,\mathrm{W\,m^{-3}}$ (corresponding to $F_{\mathrm{T}} = 1.68^{\circ}\mathrm{C\,h^{-1}}$) north of the Subpolar Front and cooling rate $(\sim -2,000\,\mathrm{W\,m^{-3}})$ south of the Subpolar Front. Near the bottom, a large cooling area with the cooling rate of $750\,\mathrm{W\,m^{-3}}$ occurs north of the Subpolar Front.

Horizontal distributions of F_{S} (unit: $\mathrm{ppt\,m^{-3}}$) on day-30 (Fig. 16.5) at the four σ levels $(0, -0.143, -0.5,$ and $-0.929)$ show near-extremely strong salinity sources/sinks generated by the diagnostic initialization. These sources/sinks have various scales and strengths. They reveal small- to meso-scale patterns in most areas but a large-scale pattern in the southern Japan/East Sea near Tsushima/Korean Strait at the surface and north of the Subpolar Front at the midlevel and bottom. The strength of the source/sink increases with depth from the surface to the bottom. The maximum salinity source (sink) is found $0.80\,\mathrm{ppt\,h^{-1}}$ $(-0.76\,\mathrm{ppt\,h^{-1}})$ at $\sigma = -0.929(\sigma = -0.5)$.

When the prognostic integration starts, the source/sink terms F_{T} and F_{S} are removed from (16.5) and (16.6). Extremely strong and spatially nonuniform initial heating/cooling (salting/freshening) rates are introduced in the
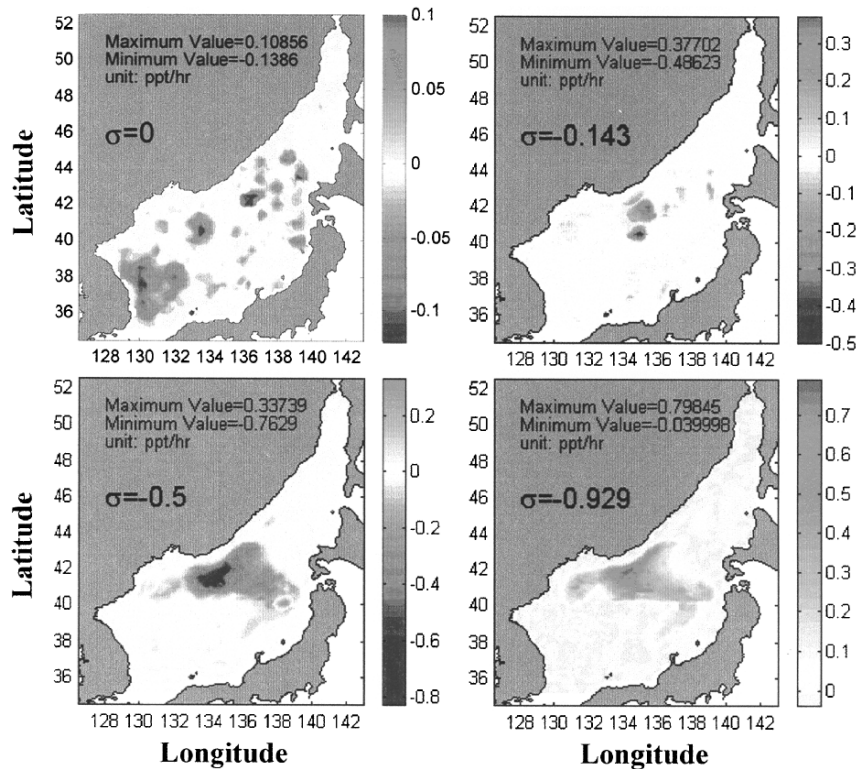
Fig. 16.5. Horizontal distribution of F_S (unit: $\mathrm{ppt\,s^{-1}}$) on day-30 at σ levels of: (**a**) 0, (**b**) -0.143, (**c**) -0.5, and (**d**) -0.929 (from Chu and Lan 2003, Geophysical Research Letters)

ocean models and cause drastic changes in thermohaline and velocity fields initially (after the diagnostic run) especially in the deep layer below the thermocline and halocline. Note that the problem is caused by the diagnostic initialization only, nothing to do with the ocean model itself.

In the diagnostic initialization, the source/sink terms drive the velocity through the pressure gradient force [see (16.1a)]. The pressure gradient error leads to errors in the initialized velocity field. Different models (z-level, σ-level, and s-level) have different pressure gradient errors, which in turns generate different initial velocity fields. Besides, the diagnostic process (spin up/down) largely depends on the diffusion. The spin down scale of 30 days is the state of balance between the pressure gradient force (not change with time) and other terms in (16.1a) such as the diffusion term that depends not only on the velocity field, but also on the model parameters. Thus, the diagnostic initialization depends on model type and model parameters.

If the diagnostic initialization continues to be used, it is urgent to study the following problems: does this artificial initial heating/cooling (salting/

freshening) induce false chaotic motion in ocean models? How long does the ocean model need to be adjusted? Does the spin-up of the prognostic run have the capability to diminish this initial effect?

If the monthly mean T_c, S_c data are used as the initial conditions, the initial heating (or cooling) and salting (or freshening) rates should not be greater than the standard measures (16.10) everywhere in the domain. If they reach the levels of strong "sources/sinks" ($|\partial T/\partial t|_{\text{Strong}}$ and $|\partial S/\partial t|_{\text{Strong}}$), the calculated $(T_c, S_c, \mathbf{V}_c, w_c)$ fields after diagnostic initialization are abnormal. If they reach the levels of extremely strong "sources/sinks" ($|\partial T/\partial t|_{\text{Extra Strong}}$ and $|\partial S/\partial t|_{\text{Extra } Strong}$), the calculated $(T_c, S_c, \mathbf{V}_c, w_c)$ fields cannot be used. Thus, development of a check-up algorithm on strength of the initial source and sink is urgent.

16.2 Uncertain Open Boundary Conditions

One difficult problem in shallow water modeling is the uncertainty of the open boundary condition. At open boundaries where the numerical grid ends, the fluid motion should be unrestricted since ideal open boundaries are transparent to motions. Two approaches, local-type and inverse-type, are available for determining open boundary condition. The local-type approach determines the open boundary condition from the solution of the governing equations near the boundary. The problem becomes selecting from a set of ad hoc open boundary conditions. Since any ad hoc open boundary condition will introduce noise into a numerical solution (Chapman 1985), it is important to choose the best one from ad hoc open boundary conditions for a particular ocean model. Without any ad hoc open boundary condition, the inverse-type approach can determine the open boundary condition from the "best" fit between model solutions and interior observations (Chu et al. 1997e). However, both methods bring considerable errors in open boundary conditions. In this section, the POM is used to illustrate the effect of uncertain open boundary condition on regional ocean prediction (Chu et al. 2005c).

16.2.1 Model Implementation

The model contains $181 \times 199 \times 23$ fixed grid points. The horizontal spacing is $5'$ latitude and longitude (approximately 5.77–7.59 km in the zonal direction and 9.265 km in the latitudinal direction) and there are 23 sigma levels in vertical coordinate. The model domain extends from 35.0 to 51.0°N, 127.0 to 142.0°E (Fig. 16.1). The horizontal friction and mixing are modeled using the Smagorinsky form with the coefficient chosen to be 0.2 for this application.

Tidal forcing was not included in this application of the model, since high frequency variability of the circulation is not considered. River outflow is also not included. However, the seasonal variation in sea surface height, temperature, salinity, circulation, and transport are represented by the model.

The atmospheric forcing includes mechanical and thermohaline forcing. The wind forcing is depicted by

$$\rho_0 K_{\mathrm{M}} \left(\frac{\partial u}{\partial z}, \frac{\partial u}{\partial z} \right)_{z=0} = (\tau_x, \tau_y), \tag{16.13}$$

where K_{M} is the vertical mixing coefficient for momentum, (u, v) and (τ_x, τ_y) are the two components of the water velocity and surface wind stress vectors, respectively. The wind stress at each time step is interpolated from monthly mean climatological wind stress from COADS (1945–1989), with a resolution of $1° \times 1°$. The COADS wind stress was interpolated into the model grid with a resolution of $5'$. Surface thermohaline forcing is depicted by

$$K_{\mathrm{H}} \frac{\partial \theta}{\partial z} \quad = \quad \alpha_1 \left(\frac{Q_{\mathrm{H}}}{\rho\, C_p} \right) + \alpha_2 C(\theta_{\mathrm{OBS}} - \theta), \tag{16.14}$$

$$K_{\mathrm{S}} \frac{\partial S}{\partial z} = -\alpha_1 F S + \alpha_2 (S_{\mathrm{OBS}} - S), \tag{16.15}$$

where K_{H} and K_{S} are the vertical mixing coefficients for heat and salt, (θ, S) and $(\theta_{\mathrm{OBS}}, S_{\mathrm{OBS}})$ are modeled and observed potential temperature and salinity, and c_p is the specific heat. (Q_H, F) are net heat and fresh water fluxes (downward positive). The parameters (α_1, α_2) are $(0, 1)$ switchers: $\alpha_1 = 0, \alpha_2 = 1$, would specify the restoring forcing; $\alpha_1 = 1, \quad \alpha_2 = 0$, would specify the flux forcing. The relaxation coefficient C is the reciprocal of the restoring time period for a unit volume of water.

Boundary conditions for closed lateral boundaries, i.e., the modeled ocean bordered by land, were defined using a free-slip condition for velocity and a zero gradient condition for temperature and salinity. Thus, no advective or diffusive heat, salt or velocity fluxes occur through these boundaries. The radiation condition (local-type approach) is used to determine T, S at the open boundaries. When the water flows into the model domain, temperature and salinity at the open boundary are prescribed from observational data. When water flows out of the domain, the radiation condition,

$$\frac{\partial}{\partial t}(\theta, S) + U_{\mathrm{n}} \frac{\partial}{\partial n}(\theta, S) \quad = \quad 0, \tag{16.16}$$

is applied. Here, the subscript n denotes the direction normal to the boundary. The temperature and salinity values at the open boundaries are obtained from monthly mean GDEM data.

For computational efficiency, the mode splitting technique (Blumberg and Mellor 1987) is applied with a barotropic time step of $25\,\mathrm{s}$, based on the CFL computational stability condition and the external wave speed; and a baroclinic time step of $900\,\mathrm{s}$, based on the CFL condition and the internal wave speed.

16.2.2 Two-Step Initialization

Two-steps are used to obtain "standard initial velocity field" for the study: presimulation and simulation. During the first step (presimulation run), POM is integrated for 2 years from zero velocity and climatological annual mean temperature and salinity fields with the monthly mean surface wind stress from the COADS data and restoring-type surface thermohaline forcing ($\alpha_1 = 0, \alpha_2 = 1$) which is relaxed to surface monthly mean values. The final states of the first step are taken as initial conditions for the second step (simulation run). During the simulation run, POM is integrated again for one and half years starting from Julian Day-1 to Julian Day-180 of the second year using the flux forcing ($\alpha_1 = 1, \alpha_2 = 0$) with monthly mean surface wind stress (τ_x, τ_y), net heat flux (Q_H), and net fresh-water flux (F) from the COADS data. The atmospheric forcing data are temporally interpolated into daily data. The final states of the simulation stage,

$$V_0 = V_{180}, \quad T_0 = T_{180}, \quad S_0 = S_{180}, \tag{16.17}$$

are taken as standard initial conditions for the numerical experiments.

16.2.3 Volume Transport at Open Boundaries

Volume transports at open boundaries are specified from historical data (Table 16.1). Positive (negative) values are referred to inflow (outflow). Warm water enters the Japan Sea through the Korea/Tsushima Strait with the Tsushima Warm Current from the East China Sea and exits the Japan Sea through the Tsugaru and Soya straits. There is no evident volume transport through the Tatar Strait (Martin and Kawase 1998), which is taken as 0. Recent estimate of the monthly mean volume transport, reported by Yi (1966), through the Korea/Tsushima Strait with the annual average of 1.3 Sv, a maximum of 2.2 Sv in October, and a minimum of 0.3 Sv in February. Bang et al. (1996) used the maximum inflow transport of about 3.5 Sv in August and minimum of 1.6 Sv in February, while Kim and Yoon (1999) used the mean value of 2.2 Sv with ± 0.35 Sv with the maximum in mid-September and the minimum in mid-March. The total inflow transport through Korea/Tsushima Straits should be the same as the total outflow transport through the Tsugaru and Soya Straits. We assume that 75% (80% in Bang et al. 1996) of the total inflow transport should flow out of the Japan/East Sea through the Tsugaru Strait, and 25% (20% in Bang et al. 1996) through the Soya Strait. This ratio is adopted from the maximum volume transport through the Tsugaru Strait estimated by Toba et al. (1982), and through the Soya Strait estimated by Preller and Hogan (1998). The monthly volume transports through open boundaries are listed in Table 16.1.

Table 16.1. Bimonthly variation of volume transport (unit: Sv)

month	Feb.	Apr.	Jun.	Aug.	Oct.	Dec.
Tatar strait (inflow)	0.05	0.05	0.05	0.05	0.05	0.05
Soya strait (outflow)	−0.1	−0.1	−0.4	−0.6	−0.7	−0.4
Tsugaru strait (outflow)	−0.25	−0.35	−0.85	−1.45	−1.55	−1.05
Tsushima strait (inflow)	0.3	0.4	1.2	2.0	2.2	1.4

16.2.4 Experimental Design

Evaluation Strategy

Ocean model output should be verified by the reality, which is represented approximately by observational (sampling) data with sufficient temporal and spatial coverage and resolution. Such a verification dataset is either not available or containing error. The initial and forcing data (wind and lateral transport) also contain error even the climatology. Difference between the model output and the observational data (if available) not only represents the model predictability but also the effect due to uncertain verification data.

In order to filter out the effect due to uncertain verification data and to quantify the uncertainty in initial and forcing data, a control run is designed with known initial condition, wind forcing, and lateral transport. The model input (initial and forcing) data are treated as "accurate." The model output data are taken as the "reality'" (i.e., the verification data without error).

Sensitivity runs are designed with quantified errors in initial condition (nonrandom error) or forcing data (random error). Comparison between the model output data and the "realty" (i.e., the output data from the control run) quantifies the two kinds of the model predictability.

Control Run

The control run is to integrate POM-Japan Sea from the standard initial conditions (16.17) for 180 days (to Julian Day-360) with the lateral transport shown in Table 16.1 (unperturbed) and the daily surface wind stress, net heat flux, and fresh-water flux interpolated from the COADS monthly mean data (unperturbed). Detailed information can be found in Chu et al. (2000c, 2001c, 2003c). The simulated surface velocity field coincides with earlier description of the Japan Sea circulation presented in Sect. 6.5.5.

Uncertain Lateral Transport

Two experiments are conducted to investigate the effect of lateral transport uncertainty. Everything keeps the same as the control run (run-0) except the bimonthly mean lateral boundary transport (see Table 16.1) where a Gaussian-type random variable is added with the zero mean and noise intensity being 5 and 10% of the transport (control run). The noise varies in two months.

Statistical Error Analysis

Difference between the horizontal velocity $\mathbf{V}$ of control run and each sensitivity run at a σ-level,

$$\Delta\mathbf{V}(x,y,\sigma,t) = \mathbf{V}c(x,y,\sigma,t) - \mathbf{V}e(x,y,\sigma,t), \qquad (16.18)$$

is defined as prediction error. Here, the subscripts (c, e) represent the control and sensitivity runs. Temporal evolution of the horizontal mean relative error is represented by the level dependent Relative Root Mean Square Error (RRMSE) between the control and sensitivity runs

$$R_1(\sigma,t) = \frac{\sqrt{\sum\limits_{i=1}^{Mx}\sum\limits_{j=1}^{My}\{[\Delta u(xi,yj,\sigma,t)]^2 + [\Delta v(xi,yj,\sigma,t)]^2\}}}{\sqrt{\sum\limits_{i=1}^{Mx}\sum\limits_{j=1}^{My}\{[u_c(xi,yj,\sigma,t)]^2 + [v_c(xi,yj,\sigma,t)]^2\}}}. \qquad (16.19)$$

Temporal evolution of the volume mean relative error is represented by the level-independent RRMSE between the control and sensitivity runs,

$$R_2(t) = \frac{\sqrt{\sum\limits_{i=1}^{Mx}\sum\limits_{j=1}^{My}\sum\limits_{k=1}^{Mz}\{[\Delta u(xi,yj,\sigma_k,t)]^2 + [\Delta v(xi,yj,\sigma_k,t)]^2\}}}{\sqrt{\sum\limits_{i=1}^{Mx}\sum\limits_{j=1}^{My}\sum\limits_{k=1}^{Mz}\{[u_c(xi,yj,\sigma_k,t)]^2 + [v_c(xi,yj,\sigma_k,t)]^2\}}}. \qquad (16.20)$$

16.2.5 Model Uncertainty

The level-dependent RRMSE, $R_1(\sigma,t)$, varies with time with smaller values on the fifth day (Fig. 16.6a) than on the 180th day (Fig. 16.6b). It increases with the noise intensity for the same (σ, t), and increases from a minimum value at the surface (0.05 for 5% noise intensity and 0.08 for 10% noise intensity on the 5th day, and 0.10 for 5% noise intensity and 0.15 for 10% noise intensity on the 180th day) to a maximum value at the bottom (0.16 for 5% noise intensity and 0.23 for 10% noise intensity on the 5th day, and 0.18 for 5% noise intensity and 0.28 for 10% noise intensity on the 180th day). Level-independent RRMSE, $R_2(t)$, oscillates with time with smaller values (0.09–0.20) for 5% noise intensity and with larger values (0.17–0.34) for 10% noise intensity (Fig. 16.7).

Since the absolute velocity can be computed from (T, S) data using the P-vector inverse method, it is possible to incorporate the P-vector algorithm into the numerical model to compute the velocity from the (T, S) values at the open boundary. This will reduce the uncertainty in the lateral boundary transport and in turn reduce the model uncertainty.
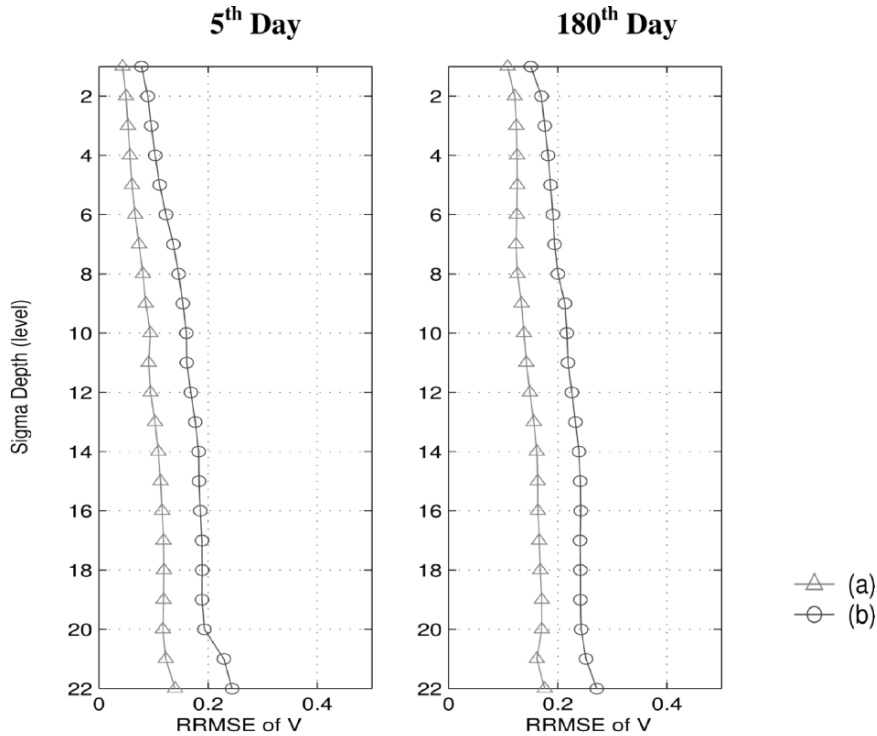
Fig. 16.6. Level dependent RRMSE due to uncertain lateral boundary transport with 5% noise intensity (represented by the symbol "Δ") and 10% noise intensity (represented by the symbol "O") on the (**a**) fifth day and (**b**) 180th day after the model integration (from Chu et al. 2005c, Continental Shelf Research)
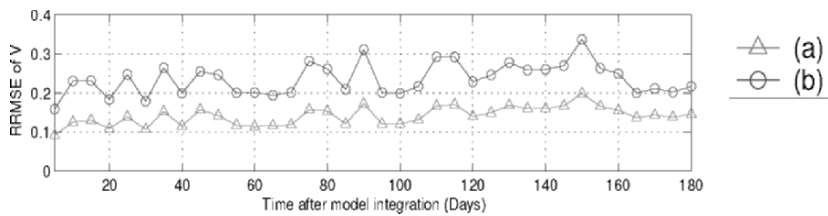

Fig. 16.7. Temporal evolution of level independent RRMSE due to uncertain lateral boundary transport with the symbol "Δ" denoting 5% noise intensity and the symbol "O" representing 10% noise intensity. Note that the error oscillates with no evident error growing trend (from Chu et al. 2005c, Continental Shelf Research)

Questions and Exercises

(1) What is the major difficulty in ocean model initialization?

(2) In ocean modeling practice, climatological (T_c, S_c) data are usually taken as the initial (T, S) conditions. Let the inverted absolute velocity from the (T_c, S_c) data be represented by $\mathbf{V}^{(p)}$. Why do the initial conditions $(T_c, S_c, \mathbf{V}^{(p)})$ satisfy the conservation of heat and salt?

(3) For the same conditions as the previous question, why do the initial conditions $(T_c, S_c, 0)$ dissatisfy the conservation of heat and salt? How strong is the artificial source/sink added to the system?

(4) Is diagnostic initialization (popularly used) feasible in ocean modeling practice? Why?

(5) Figures 16.4 and 16.5 show large artificial heat and salt sources/sinks during the diagnostic initialization. Discuss the effect of this extra thermohaline forcing on the model results.

(6) Discuss the two types of model predictability using the POM-Japan/East Sea model.

(7) Select a region and a numerical ocean model of your interest. The annual mean WOA (T_c, S_c) data are used. The corresponding absolute velocity $(\mathbf{V}^{(p)}$ data are downloaded from the enclosed CD-ROM. Run the POM diagnostic mode with the fixed (T_c, S_c) fields for periods of time (30, 60, 90 days) to get velocity fields $(\mathbf{V}_{30}, \mathbf{V}_{60}, \mathbf{V}_{90})$. Analyze the difference between $\mathbf{V}^{(p)}$ and $(\mathbf{V}_{30}, \mathbf{V}_{60}, \mathbf{V}_{90})$.

(8) Run the numerical model from the initial conditions $(T_c, S_c, \mathbf{V}^{(p)})$ for a year as the control case. Run the numerical model from the initial conditions $(T_c, S_c, \mathbf{V}_{30})$, $(T_c, S_c, \mathbf{V}_{60})$, and $(T_c, S_c, \mathbf{V}_{90})$ for a year as the sensitivity cases. Analyze the difference between the control and sensitivity cases. Report the results.